

Curve-Induced Dynamical Systems on Riemannian Manifolds and Lie Groups

Saray Bakker^{*1}, Martin Schonger^{*2,3}, Tobias Löw^{2,3}, Javier Alonso-Mora¹ and Sylvain Calinon²

Abstract—Deploying robots in household environments requires safe, adaptable, and interpretable behaviors that respect the geometric structure of tasks. Often represented on Lie groups and Riemannian manifolds, this includes poses on $SE(3)$ or symmetric positive definite matrices encoding stiffness or damping matrices. In this context, dynamical system-based approaches offer a natural framework for generating such behavior, providing stability and convergence while remaining responsive to changes in the environment. We introduce Curve-induced Dynamical systems on Smooth Manifolds (CDSM), a real-time framework for constructing dynamical systems directly on Riemannian manifolds and Lie groups. The proposed approach constructs a nominal curve on the manifold, and generates a dynamical system which combines a tangential component that drives motion along the curve and a normal component that attracts the state toward the curve. We provide a stability analysis of the resulting dynamical system and validate the method quantitatively. On an S^2 benchmark, CDSM demonstrates improved trajectory accuracy, reduced path deviation, and faster generation and query times compared to state-of-the-art methods. Finally, we demonstrate the practical applicability of the framework on both a robotic manipulator, where poses on $SE(3)$ and damping matrices on S_{++}^n are adapted online, and a mobile manipulator.

Index Terms—Dynamical Systems, Riemannian Manifolds, Lie Groups

I. INTRODUCTION

Real-world deployment of robots in household settings requires systems that are inherently safe, adaptable, and interpretable. Achieving such safe and reliable behavior requires models that respect the underlying structure of the complex tasks these robots perform. In many cases, the processed data is inherently non-Euclidean, residing on curved manifolds rather than in standard vector spaces. Considering the geometry of the task, such as poses on $SE(3)$, or stiffness and damping expressed as symmetric positive definite (SPD) matrices on S_{++}^n , is crucial for effective task execution as well as safety during interaction. For instance, in a robot-assisted dressing task, as shown in Fig. 1, the robot adapts

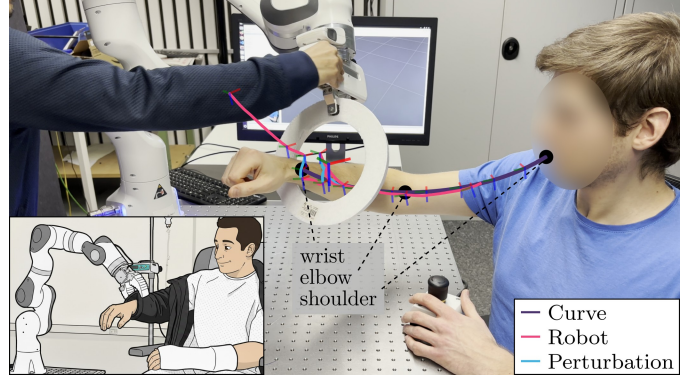


Fig. 1: We consider a dressing task in which the robot adapts both its pose and the damping matrix of an impedance controller throughout the motion. External perturbations are applied by physically pushing the robot, and we observe that the proposed CDSM converges back to the desired nominal trajectory, given the tracked configuration of the human arm via a camera. The illustration in the bottom-left corner was generated using Google Gemini.

its end-effector pose to the human arm's configuration and varies the affine transformation for the desired velocity in the impedance controller, hereafter referred to as the damping matrix, throughout the interaction.

Dynamical system-based approaches offer an appealing framework for generating robot behavior in such settings, as they can provide formal guarantees on stability and convergence while remaining highly reactive to changes in the environment. Several approaches have been developed, ranging from learning-based to deterministic methods.

Recently, there has been growing interest in learning stable dynamical systems (DSs) on Riemannian manifolds and Lie groups. A prominent line of work leverages normalizing flows as diffeomorphic mappings, both for Lie groups [1] and for more general Riemannian manifolds [2]. Closely related approaches employ Flow Matching on Riemannian manifolds [3], [4] or enforce stability explicitly through constraints in the loss function [5]. Broadly speaking, data-driven methods still make specific assumptions to achieve stability that could limit performance on manifolds. They typically require several demonstrations, and training times hinder real-time adaptation of the learned DS to changes in the environment or task, such as adapting to different human arm configurations in the dressing task. In addition, convergence in a learned DS is typically directed towards the goal, rather than the demonstrated trajectories, even though explicitly attracting the system to those trajectories could improve user-interpretability and task

*These authors contributed equally and are mentioned in alphabetic order.

The authors are associated with 1. Delft University of Technology, The Netherlands, 2. Idiap Research Institute, Switzerland, and 3. École Polytechnique Fédérale de Lausanne (EPFL), Switzerland.

This project has received funding from the European Union through ERC, INTERACT, under Grant 101041863, and the Swiss National Science Foundation (SNSF) through the HORACE project (Grant 10002813, horace-robotics.github.io). Views and opinions expressed are those of the author(s) and do not necessarily reflect those of the granting authority. Neither the European Union nor the granting authority can be held responsible for them.

Project website and video: cd-sm.github.io.

Corresponding authors: Saray Bakker (s.bakker-7@tudelft.nl) and Martin Schonger (martin.schonger@epfl.ch).

execution, especially when working with a small dataset.

This motivates the use of vector-field-based approaches defining a reference curve and constructing a vector field that draws motion toward this curve while also steering it along the curve’s direction. These curves can be constructed as motion primitives (MPs), an effective and lightweight approach to encode a trajectory or data sequence, which can be defined on Riemannian manifolds and Lie groups [6], [7]. In Euclidean space, Li and Calinon [8] show that an analytic distance map can be generated when using composite quadratic Bézier curves, and converted into a dynamical system to react to disturbances. Although extensions to Riemannian manifolds are proposed, applying the approach to arbitrary demonstrated trajectories remains nontrivial [9], or, relies on projecting actions from \mathbb{R}^n onto the tangent spaces of the manifold without explicitly accounting for the geometric structure to construct a dynamical system on the manifold [10].

We propose Curve-induced Dynamical systems on Smooth Manifolds (CDSM), which consists of a dynamical system formulation on Riemannian manifolds and an extension to Lie groups, naturally handling robotic data such as varying damping matrices, poses, and orientations, while maintaining reactivity and practical stability. Building on the Euclidean-space DS in [8], we leverage tools from differential geometry to generate a stable DS converging to a curve for Riemannian manifolds, such as S^2 and S_{++}^n -matrices, and Lie groups, such as $SO(3)$ and $SE(3)$. In particular, gain matrices of an impedance controller can be represented as *full* S_{++}^6 -matrices [11], enabling extensions beyond approaches that leverage *diagonal* stiffness and damping matrices [12], [13]. The curve is built from single or multiple demonstrated trajectories or data-sequences, thereby ensuring C^1 -continuity. We provide fast curve optimization as well as batch evaluation and forward simulation of the DS using JAX [14], [15]. Moreover, we propose a coupling between a spatial profile, encoding poses, and a curve of S_{++}^6 matrices, encoding damping matrices. Our approach is able to compute both the parametrized curves as well as actions of the DS in real-time, making it well-suitable for several real-world tasks such as the dressing task in Fig. 1, where high responsiveness to changes of the arm configuration and disturbances is required.

Additionally, to extend the adaptability of the CDSM framework, we introduce a phase modulation layer on top of the reference data-based trajectory profile, leveraging the same parametric curve structure. This structure enables flexible adaptation of the system’s timing. For instance, the phase profile can be optimized given velocity constraints or to increase reactivity to dynamic obstacles or agents, without altering the spatial curve itself. By decoupling timing from the curve, CDSM can adapt its execution speed and responsiveness while preserving the learned motion’s shape.

Our contributions are as follows:

- A curve-induced dynamical system-formulation suitable for Riemannian manifolds and an extension to Lie groups, which can be constructed from a single or multiple demonstrated trajectories, or data sequences in real-time.
- Coupling a CDSM of poses in $SE(3)$ with a curve of full S_{++}^n matrices encoding variable Cartesian damping

matrices by synchronizing their phase profiles.

- Combining CDSM with a phase modulation layer to enable adaptive timing, illustrated by an example imposing speed constraints.
- Quantitative experiments of our approach compared against LiefloWS [1] and PUMA [5] on the LASA dataset mapped to S^2 , and real-world deployment for a human-arm dressing task on a manipulator, as well as on a mobile manipulator.

Our code will be released open-source upon publication, including examples of CDSM on several types of Riemannian manifolds and Lie groups, including S^2 , $SO(3)$, $SE(3)$, and S_{++}^n up to $n = 6$.

II. RELATED WORK

In this section, we analyze several DS-based approaches for generating stable motions on smooth manifolds, ranging from deep-learning based approaches to guiding vector fields.

A. Learning Stable Dynamical Systems on Manifolds

Recently, several methodologies have been proposed for incorporating safety and stability guarantees leveraging learned dynamical systems [16]. By leveraging Neural ODEs, normalizing flows learn a diffeomorphic mapping between the observation space and latent space to generate a stable vector field, ensuring stability by connecting the task-space system to a simple, stable latent-space dynamical system. The method has been generalized to Lie groups [1] and Riemannian manifolds [2]. Flow Matching [17] trains a Continuous Normalizing Flow resulting in a simplified procedure and better scalability compared to the likelihood maximization used in normalizing flows, and has been extended to several types of Riemannian manifolds [3], [4]. Learning a bijective mapping to a simple hand-defined system in the latent space can be restrictive especially for non-Euclidean data. By enforcing stability of the DS via an additional term in the loss function, Pérez-Dattari et al. [5] avoid mapping to a simple system, and showcase its performance on S^2 and $SE(3)$ -manifolds. Diffusion policies, on the other hand, have the potential to handle multimodal distributions, and are demonstrated on $SE(3)$ in [18]. However, diffusion policies do not provide formal safety and stability guarantees.

All learning-based methods mentioned above require a training procedure that typically ranges from several minutes to hours. By contrast, small-scale parametric models such as Gaussian Mixture Models (GMMs) can learn diffeomorphic mappings for motions on Riemannian manifolds [19], with training procedures that can be executed in real time. However, ensuring that the learned diffeomorphism is sufficiently expressive, bijective, and smoothly invertible remains challenging, and often imposes restrictive design constraints, particularly when such mappings are applied on Riemannian manifolds.

B. Dynamical Systems on Non-Euclidean Spaces

Deterministic trajectory generation methods on smooth manifolds that do not rely on learning-based pipelines have

been extensively studied. This includes work on second-order nonlinear oscillators defined directly on manifolds [20], as well as Dynamic Motion Primitives (DMPs) adapted to non-Euclidean spaces. In particular, DMP formulations have been proposed for orientations using unit quaternions [21], [22], for poses [23], and more generally for Riemannian manifolds, including the space of \mathcal{S}_{++}^n -matrices [24]. A probabilistic extension of DMPs for orientations represented by unit quaternions was introduced in [25]. These second-order nonlinear oscillators and DMPs primarily focus on reproducing a single nominal trajectory on the manifold. In contrast, our work targets not only accurate trajectory generation but also reactive behavior under disturbances and robust performance in regions of the manifold that are distant from the demonstrated or prescribed trajectory.

To enable robust and safe motion generation from off-trajectory conditions, vector fields and dynamical systems are proposed, including guiding vector fields [26], [27], velocity fields for contour following [28], and stable dynamical systems [8], [29]. These approaches typically define an action by combining an attraction term towards the curve with a continuation term following the movement profile of the demonstrated trajectory or movement towards the global goal. However, such formulations are generally developed in Euclidean spaces. When naively extended to Riemannian manifolds or Lie groups via a single tangent-space projection, they can lead to significant geometric distortions [30].

In [9], a convergence and stability analysis of guiding vector fields on Riemannian manifolds is provided. Given an n -dimensional configuration space, their approach constructs a reference path as an intersection of $(n - 1)$ -dimensional zero-level sets, to which the vector field should converge. Although they thoroughly analyze the difficulties of achieving global asymptotic stability for curves homeomorphic to the unit circle, their focus on examples with hand-defined and elementary curves limits the direct applicability of their results to the complex geometric structures encountered in robotic tasks. For an arbitrary demonstrated trajectory, it remains nontrivial to define the desired path as an intersection of zero-level sets, and it becomes challenging to separate the attraction and progression component with respect to the original path, from the vector field directing towards the zero-level sets.

A more practical approach is the vector field proposed in [10], which combines attractive and demonstration-following velocities on Riemannian manifolds, and demonstrates a learning-based extension on a real-world robotic umbrella-hanging task. However, compared to our approach, the DS in [10] still requires a projection of the output of the vector field or learned vector field, which lies in \mathbb{R}^n , into the local tangent space of the manifold, while our approach explicitly constructs the DS to output vectors that lie in the tangent spaces of the manifold. Finally, by fitting a continuous curve, rather than directly converging to a demonstrated trajectory as in [10], our approach ensures C^1 -continuous motions along the curve and a dynamical system that progresses towards the goal, without requiring such regularity to be present in the original demonstration.

III. PRELIMINARIES

A. Riemannian Manifolds

Let M be a smooth manifold of dimension n . Locally, the manifold resembles the Euclidean space \mathbb{R}^n , but globally it may have a complex topological structure. At every point $p \in M$, we associate an n -dimensional vector space T_pM called the *tangent space*. Intuitively, this space consists of all possible tangent vectors to curves passing through p . Formally, if $\gamma: (-\epsilon, \epsilon) \rightarrow M$ is a smooth curve with $\epsilon > 0$ and $\gamma(0) = p$, the velocity vector $\dot{\gamma}(0)$ is an element of T_pM [31]. The collection of all tangent spaces forms the *tangent bundle*, denoted $TM = \bigsqcup_{p \in M} T_pM$. A *vector field* X on M is a smooth section of this bundle; it assigns a tangent vector $X_p \in T_pM$ to every point p in a smooth manner. The space of smooth vector fields is denoted by $\mathfrak{X}(M)$.

A *Riemannian manifold* is a pair (M, g) , where g is a *Riemannian metric*. When g is clear from context, we simply refer to M . The metric g is a smooth field of inner products, assigning to each $p \in M$ a symmetric, positive-definite bilinear form $\langle \cdot, \cdot \rangle_p: T_pM \times T_pM \rightarrow \mathbb{R}$. This allows us to define the length of tangent vectors as $\|v\|_p = \sqrt{\langle v, v \rangle_p}$.

The metric induces a unique torsion-free affine connection ∇ , called the *Levi-Civita connection* [32]. This connection allows us to differentiate vector fields and compare tangent vectors at different points. Given a curve $\gamma: [t_0, t_1] \rightarrow M$, the connection defines a linear isometry known as *parallel transport*, which preserves inner products along the curve. A *geodesic* is a locally length-minimizing curve γ with zero acceleration. For parallel transport along the unique geodesic connecting $p \in M$ to $q \in M$, we use the notation:

$$\mathcal{P}_{p \rightarrow q}: T_pM \rightarrow T_qM. \quad (1)$$

The *exponential map*,

$$\exp_p: T_pM \rightarrow M, \quad (2)$$

maps a tangent vector $v \in T_pM$ to the point on the manifold reached by the geodesic starting at p with velocity v after one unit of time. The *logarithmic map*,

$$\log_p: M \rightarrow T_pM, \quad (3)$$

is the *local* inverse of the exponential map. It maps a point $q \in M$ to the tangent vector in T_pM representing the initial velocity of the geodesic connecting p to q .

The *Riemannian distance*, or geodesic distance, is defined intrinsically via the logarithm:

$$d_M(p, q) = \|\log_p(q)\|_p. \quad (4)$$

B. Lie Groups

A *Lie group* G is a smooth manifold that is also a group in the algebraic sense, with smooth multiplication, $m: G \times G \rightarrow G, (g, h) \mapsto gh$, and inverse maps, $i: G \rightarrow G, g \mapsto g^{-1}$, respectively [33]. For any fixed element $g \in G$, the *left translation* map $L_g: G \rightarrow G$ is defined by $L_g(h) = gh$. Since G is a smooth manifold, we can consider the differential of this map, often called the *pushforward*, at any point $h \in G$. We denote this pushforward by $d(L_g)_h: T_hG \rightarrow T_{gh}G$. It is

a linear map that transports tangent vectors from the tangent space at h to the tangent space at gh , preserving the group structure. A vector field $X \in \mathfrak{X}(G)$ is called *left-invariant* if it is preserved by the pushforward of left translations. Formally, for all $g, h \in G$, the field must satisfy $d(L_g)_h(X_h) = X_{gh}$. Here, X_h denotes the value of the vector field X evaluated at point h . The condition states that if we take the vector at h and push it forward by left-multiplying by g , we obtain exactly the vector assigned by the field at the point gh .

The *Lie algebra* \mathfrak{g} of G is the space of all left-invariant vector fields on G , equipped with the Lie bracket operation $[X, Y]$. As a vector space, it is standard to identify \mathfrak{g} with the tangent space at the identity, $T_e G$. The *Lie group exponential*,

$$\exp: \mathfrak{g} \rightarrow G, \quad (5)$$

maps lines in the algebra to one-parameter subgroups in the group. Since the exponential map is not necessarily injective, it does not have a global inverse. The *Lie group logarithm*,

$$\log: U \subseteq G \rightarrow \mathfrak{g}, \quad (6)$$

is defined as the diffeomorphism inverse of \exp restricted to a sufficiently small neighborhood U of the identity element e . Distances can be defined via the Lie group logarithm,

$$d_G(g, h) = \|\log(g^{-1}h)\|_{\mathfrak{g}}, \quad (7)$$

where $\|\cdot\|_{\mathfrak{g}}$ denotes a suitable weighted norm on the Lie algebra to handle unit discrepancies.

IV. CURVE-INDUCED DYNAMICAL SYSTEMS ON RIEMANNIAN MANIFOLDS AND LIE GROUPS

Let M be a smooth, finite-dimensional, connected, and complete Riemannian manifold. Given reference data, we want to fit a smooth non-self-intersecting curve $\gamma: [0, 1] \rightarrow M$ on the data, and construct an *autonomous continuous-time DS* of the form,

$$\dot{x}(t) = f(x(t)), \quad (8)$$

with the equilibrium point $x^* = \gamma(1)$, such that $f(x^*) = 0$, where 0 denotes the zero vector of appropriate dimension. The objective is to guide the system state $x(t) \in M$ to converge to γ and propagate along it toward x^* . We want f to be sufficiently smooth such that for any initial condition $x(0) = x_0 \in \mathcal{D} \subseteq M$, a unique solution $x(t)$ exists for all $t \geq 0$, where the domain \mathcal{D} depends on the global geometry of the pair (M, γ) .

Where appropriate, we point out differences when dealing with a Lie group G instead of a Riemannian manifold M . If not specified otherwise, one may simply replace M by G , and d_M by d_G , as well as apply group operations accordingly. Further, instead of tangent vectors one would then deal with Lie algebra elements.

In the following subsections we first explain how such curve γ can be obtained from reference data in Section IV-A. Then, we discuss the construction of a DS, $f(x(t))$, based on this curve or any given curve that is smooth and non-self-intersecting in Section IV-B, provide an analysis of the stability of the DS, and explain the phase modulation layer. In

Section V, additional details are provided for generating the proposed CDSM on manifolds relevant for robotics, along with an example for connecting DSs and curves, e.g. connecting a DS of $SE(3)$ poses with variable Cartesian damping matrices.

A. Constructing Curves on Manifolds

Given reference data, such as user-demonstrated trajectories or data obtained from an optimal control problem, we can fit a curve γ defined by a set of parameters Θ , i.e. $\gamma(s; \Theta)$. Without loss of generality, we may assume the phase-variable s to be in the domain $s \in [0, 1]$, as we can scale inputs to γ and curve derivatives accordingly. More formally, consider a set of $K \in \mathbb{N}^+$ individual data sequences, $X^{\text{ref}} = \bigcup_{k=1}^K \{(k, s_i^k, x_i^k)\}_{i=1}^{I_k}$, where I_k denotes the number of samples in the k -th data sequence. The parameters Θ of γ can then be found by minimizing the distance on the manifold between the curve and the data-points:

$$\underset{\Theta}{\operatorname{argmin}} \sum_{k=1}^K \sum_{i=1}^{I_k} d_M(\gamma(s_i^k; \Theta), x_i^k)^2. \quad (9)$$

As a concrete realization of curves on manifolds, we consider composite quadratic Bézier curves, building on the Euclidean formulation in [8]. To avoid distortion, the curves must fit the reference data directly on the manifold rather than in a tangent space. Tangent spaces are nonetheless used to encode individual quadratic segments, where construction is straightforward [7], while curve evaluation, continuity constraints, and the distances in (9) are defined on the manifold. As the basis for a segment's tangent space, we use the first control point of the respective segment.

Specifically, for $j \in \{1, 2, \dots, J\}$ with J the number of segments, we encode the quadratic segment $u_j(s)$ in the tangent space at base point $p_j \in M$. Given a local phase $s_j \in [0, 1]$, the segment is defined as,

$$u_j(s_j) = (1 - s_j)^2 w_{1,j} + 2(1 - s_j)s_j w_{2,j} + s_j^2 w_{3,j}. \quad (10)$$

Here, the inputs and curve derivatives are rescaled to express $u_j(s)$ in terms of the global phase s , assuming all J segments have equal duration. The control points $w_{i,j}, \forall i \in \{1, 2, 3\}$, are expressed in this tangent space $T_{p_j}M$, with $w_{1,j} = 0$ being at its origin, see Fig. 2. The curve $u_j(s)$, defined in the tangent space, is then mapped back to a curve $\gamma_j(s)$ on the manifold,

$$\gamma_j(s) = \exp_{p_j}(u_j(s)). \quad (11)$$

To achieve C^0 continuity, the last control point of segment j must correspond to the same point on the manifold as the first control point of the next segment,

$$p_{j+1} = \exp_{p_j}(w_{3,j}), \quad (12)$$

where we note that $\exp_{p_{j+1}}(w_{1,j+1}) = \exp_{p_{j+1}}(0) = p_{j+1}$,

For C^1 continuity, the vectors $v_{2,j}$ and $v_{1,j+1}$ lying in different tangent spaces, $T_{p_j}M$ and $T_{p_{j+1}}M$, respectively, with $v_{i,j} = w_{i+1,j} - w_{i,j}$ being the direction vector between two consecutive control points, must satisfy the constraint:

$$v_{1,j+1} = \mathcal{P}_{p_j \rightarrow p_{j+1}}(v_{2,j}). \quad (13)$$

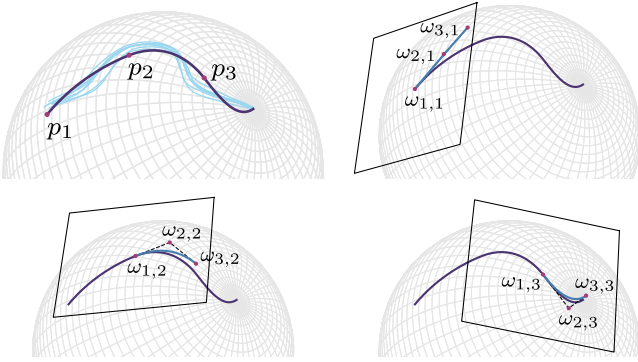


Fig. 2: Curve on S^2 with an illustration of the curve segment definitions and control points in multiple tangent spaces. The top left shows the segment base points on the manifold, as well as the reference data in light blue. Here, the curve is encoded with only 3 segments for better visualization of the procedure.

For Lie groups, instead of multiple tangent spaces we use coordinate transformations in the form of left translations to the individual segments' base points, i.e. the segments' first control points. Further, $\exp_{p_j}(\cdot)$ becomes $p_j \exp(\cdot)$.

The final composite curve γ is composed of the set of all the individual curves $\{\gamma_j(s)\}_{j=1}^J$, with their phase scaled by $1/J$:

$$\begin{aligned} \gamma(s) &= \gamma_j(s/J), \quad s \in [0, 1], \\ \text{with } j &= \min\{\lfloor sJ \rfloor + 1, J\}. \end{aligned} \quad (14)$$

With Θ being the set of all segments' control points, we can instantiate and solve the optimization problem (9), subject to the constraints (12) and (13).

B. Dynamical System Construction

Equipped with a curve γ , we want to define a dynamical system that balances attraction towards the curve and continuation along the curve direction. For this, we require the closest point on the curve given a query point on the manifold.

Definition IV.1 (Closest Point Projection). For any state $x \in M$, we define the projection map $\pi: M \rightarrow \gamma$ as the point on the curve γ minimizing the geodesic distance:

$$\pi(x) = \gamma(\tilde{s}(x)), \quad \text{where } \tilde{s}(x) = \underset{s \in [0,1]}{\operatorname{argmin}} d_M(x, \gamma(s)). \quad (15)$$

This map is well-defined and smooth on the domain $\mathcal{D} = M \setminus \mathcal{C}_{\text{sing}}$, where $\mathcal{C}_{\text{sing}}$ denotes the *cut locus* of the curve γ . $\mathcal{C}_{\text{sing}}$ is the set of all points $x \in M$ where the distance minimizer to γ is not unique, or, in other words, it represents the set of points where the closest-point projection is ill-posed. This set encapsulates singularities arising from both the local curvature of the embedding (e.g., focal points) and the global topology of the manifold (e.g., antipodal sets). Whenever a projection is not unique, we can choose the largest phase \tilde{s} out of all points on the curve $\gamma(s)$ with minimal distance from the query point x .

Since the optimization problem encapsulated by π in (15) is on a one-parameter curve, it is straightforward and efficient to solve. Fig. 3a shows a curve and its distance field along with some closest point projections on the S^2 -manifold. Note

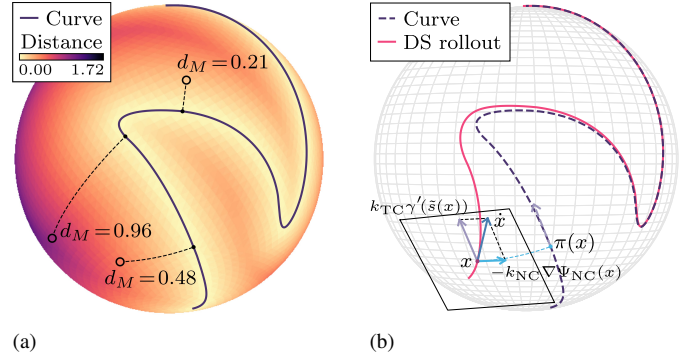


Fig. 3: (a) Distance field for a curve on S^2 with examples of projections and geodesic distances on the manifold. (b) A trajectory of the DS converging towards the curve with the tangential (TC) and normal (NC) term of the DS in the tangent space at the query point. The velocities are scaled for the illustration.

that this distance *field* is purely illustrative as our method only requires to perform the closest point projection for the current query point.

Given a curve γ and the projection operator π from Definition IV.1, we define a DS as the superposition of a term *tangential* to γ (TC; to propagate along the curve) and a term *normal* to γ (NC; to eliminate cross-track error).

Definition IV.2 (Dynamical System). For all $x \in \mathcal{D}$, the closed-loop DS is governed by:

$$\dot{x} = f(x) := \underbrace{k_{\text{TC}} \mathcal{P}_{\pi(x) \rightarrow x}(\gamma'(\tilde{s}(x)))}_{\text{Propagation}} - \underbrace{k_{\text{NC}} \nabla \Psi_{\text{NC}}(x)}_{\text{Convergence}}, \quad (16)$$

where $k_{\text{TC}}, k_{\text{NC}} > 0$ are positive scalar gains, $\pi(x) = \gamma(\tilde{s})$ is the closest point on the curve to x according to (15), $\gamma'(\tilde{s}) \in T_{\pi(x)}M$ is the velocity of the curve at $\pi(x)$ pointing along the curve, and $\mathcal{P}_{\pi(x) \rightarrow x}$ transports $\gamma'(\tilde{s})$ along the geodesic from $\pi(x)$ to x . The normal energy potential is

$$\Psi_{\text{NC}}(x) = \frac{1}{2} d_M^2(x, \pi(x)). \quad (17)$$

Its negative gradient, $-\nabla \Psi_{\text{NC}}(x)$, corresponds to the tangent vector at x of the geodesic connecting x to $\pi(x)$, and points towards the curve.

The propagation term represents the tangential desired velocity $\gamma'(\tilde{s})$ at the current point x , while the convergence term drives the system towards the curve. By the First Variation of Arc Length (Gauss's Lemma) [32], these two vectors are orthogonal at x where $\tilde{s}(x) \in (0, 1)$, which ensures that the propagation term does not degrade the convergence to the curve. For Lie groups, the propagation term, without k_{TC} , corresponds to the Lie algebra element, $\log(\gamma(\tilde{s})^{-1} \gamma'(\tilde{s}))$. The negative gradient of the normal energy potential corresponds to the Lie algebra element $\log(x^{-1} \pi(x))$.

Note a crucial difference to the approach in Euclidean space as described in [8]. In Euclidean space, the propagating velocity vector on the curve, $\gamma'(\tilde{s})$, can be directly applied to x as the tangential velocity vector. In our case of Riemannian manifolds, $\gamma'(\tilde{s})$ is initially computed in the tangent space at

$\pi(x)$, while the final command needs to be expressed in the tangent space at x , i.e. $\mathcal{P}_{\pi(x) \rightarrow x}(\gamma'(\tilde{s}))$.

1) *Behavior Towards Goal*: In order to ensure that the DS gracefully comes to a stop at the final point on the curve, $\gamma(1)$, independently of the provided reference data, we scale the tangential vector to zero as we approach the goal. This is done by defining the gain function k_{TC} in (16) as

$$k_{\text{TC}}(\tilde{s}) = k_{\text{TC}}^c \zeta(\tilde{s}), \text{ where } \zeta(\tilde{s}) = (1 - \tilde{s}^{k_g}), \quad (18)$$

with positive constant $k_{\text{TC}}^c > 0$, and configuration parameter $k_g > 1$. A smaller value for k_g means that the scaling to zero becomes more significant further away from the goal. Since ζ is smooth with $0 \leq \zeta \leq 1$, it only achieves a phase reparameterization and does not affect the system's stability.

2) *Generic Riemannian Manifolds*: In Definition IV.1 and IV.2, we assume that distances on a Riemannian manifold or Lie group can be obtained, either analytically or numerically, and that both distance and transport operations are feasible in real time. This assumption is valid for many manifolds commonly used in robotics, as demonstrated in our examples for S^2 , $SO(3)$, $SE(3)$, and S_{++}^n . For general Riemannian manifolds, closed-form solutions for these operations may not exist, often requiring iterative integration or optimization. Nevertheless, by leveraging JAX, these computations can be executed with sufficient efficiency to enable near real-time performance. When efficient distance computations are infeasible for the respective manifold, distances can be evaluated in local tangent spaces, providing an alternative to computing them directly on the manifold, although, under the risk of severe distortions.

C. Stability Analysis

Formally proving global asymptotic stability (GAS) for DSs on Riemannian manifolds remains challenging and can be proven to be impossible for specific curves or manifolds, as stated in [9]. For example, the Lie group $SO(3)$ is double covered by unit quaternions, meaning that two distinct quaternions, q and $-q$, represent the same rotation in $SO(3)$ which results in the *unwinding problem* where the system unwinds a full rotation instead of taking the shortest path. In addition, the curve $\gamma(s)$ will likely cause singular points or singular regions in the DS, and trajectories could exist that converge to the singular set instead of the curve (see the example in Fig. 5.6 in [9]). We will therefore analyze the *practical stability* of the DS, which implies that under some assumptions the DS will converge to the equilibrium $x^* = \gamma(1)$.

Let us consider the system $\dot{x} = f(x)$ on the complete, connected Riemannian manifold M as stated in Definition IV.2. As defined in Section IV-B, the domain \mathcal{D} excludes the cut locus $\mathcal{C}_{\text{sing}}$ of the curve γ . On \mathcal{D} , we propose the Lyapunov candidate,

$$V(x) = k_{\text{NC}} \Psi_{\text{NC}}(x) + k_{\text{TC}} \Psi_{\text{TC}}(x), \quad (19)$$

$$\text{where } \Psi_{\text{TC}}(x) = \frac{1}{2} (1 - \tilde{s}(x))^2,$$

with phase $\tilde{s}(x)$ as in (15), and proceed to demonstrate how practical stability is achieved with this Lyapunov candidate.

For a 1D curve on an n -dimensional manifold, $\mathcal{C}_{\text{sing}}$ is a stratified set of dimension at most $n - 1$, and thus has measure zero. Geometrically, this set forms the ‘‘ridges’’ of the distance potential Ψ_{NC} . In directions transversal to these ridges, the distance potential is concave, i.e. the ridges are local maxima. This implies that the Hessian of the distance potential possesses negative eigenvalues at critical points within $\mathcal{C}_{\text{sing}}$ [34]. Consequently, these points represent unstable equilibria of the distance potential Ψ_{NC} . Since the ridges of the distance potential do not coincide with the curve γ , and Ψ_{TC} in (19) does not induce local minima on these ridges, the DS is non-attractive to $\mathcal{C}_{\text{sing}}$, and therefore no trajectories exist that converge to the set $\mathcal{C}_{\text{sing}}$. Moreover, we assume that no trajectory passes through this zero-measure set. In other words, we assume that trajectories starting in the domain $\mathcal{D} = M \setminus \mathcal{C}_{\text{sing}}$, stay in \mathcal{D} . It therefore only holds to show that on \mathcal{D} , the DS converges to the equilibrium $x^* = \gamma(1)$. To this end, we will demonstrate that the Lyapunov candidate $V(x)$ in (19) is positive definite, proper and dissipative on \mathcal{D} .

Positive Definiteness: By definition, the convergence term $\Psi_{\text{NC}}(x)$ is equal to zero on the curve, i.e. $\Psi_{\text{NC}}(x) = 0, \forall x \in \gamma$, and larger than zero when not on the curve, i.e. $\Psi_{\text{NC}}(x) > 0, \forall x \notin \gamma$. The term $\Psi_{\text{TC}}(x)$ is nonnegative, with equality to zero iff $\tilde{s} = 1$. Thus, $V(x) \geq 0$, and $V(x) = 0$ iff $x = \gamma(1)$.

Properness: We assume that the manifold M is compact, which implies that the sublevel sets of V are compact. For non-compact manifolds like $SE(3)$, this property only holds when restricting the analysis to a bounded subset, which is a valid assumption for the workspace of a robotic manipulator.

Dissipation: We compute the time derivative along the trajectories. Using \dot{x} given by the DS in (16) and the chain rule on the Riemannian manifold [35]:

$$\dot{V} = \langle \nabla V, \dot{x} \rangle \quad (20a)$$

$$= \langle k_{\text{NC}} \nabla \Psi_{\text{NC}} + k_{\text{TC}} \nabla \Psi_{\text{TC}}, \dot{x} \rangle - k_{\text{NC}} \nabla \Psi_{\text{NC}} + k_{\text{TC}} \mathcal{P}_{\pi(x) \rightarrow x}(\gamma'). \quad (20b)$$

We substitute the tangential gradient $\nabla \Psi_{\text{TC}} = -\frac{1-\tilde{s}}{\beta(x)} \mathcal{P}_{\pi(x) \rightarrow x}(\gamma')$, where $\beta(x)$ accounts for the metric distortion in the tubular neighborhood [36], [32]. Expanding the inner product yields:

$$\begin{aligned} \dot{V} = & -k_{\text{NC}}^2 \langle \nabla \Psi_{\text{NC}}, \nabla \Psi_{\text{NC}} \rangle \\ & + k_{\text{NC}} k_{\text{TC}} \underbrace{\langle \nabla \Psi_{\text{NC}}, \mathcal{P}_{\pi(x) \rightarrow x}(\gamma') \rangle}_{\text{Term A}} \\ & - k_{\text{NC}} k_{\text{TC}} \frac{1-\tilde{s}}{\beta(x)} \underbrace{\langle \mathcal{P}_{\pi(x) \rightarrow x}(\gamma'), \nabla \Psi_{\text{NC}} \rangle}_{\text{Term B}} \\ & - k_{\text{TC}}^2 \frac{1-\tilde{s}}{\beta(x)} \underbrace{\langle \mathcal{P}_{\pi(x) \rightarrow x}(\gamma'), \mathcal{P}_{\pi(x) \rightarrow x}(\gamma') \rangle}_{\text{Term C}}. \end{aligned} \quad (21)$$

Orthogonality: By the First Variation of Arc Length (Gauss’s Lemma), the geodesic radius vector, and thus $\nabla \Psi_{\text{NC}}$, is strictly orthogonal to the parallel transported tangent vector $\mathcal{P}_{\pi(x) \rightarrow x}(\gamma')$, for x with $\tilde{s} \in (0, 1)$ on \mathcal{D} . Consequently, both cross-terms, Term A and Term B, vanish for $\tilde{s} \in (0, 1)$. For points x projecting towards the end of the curve, $\tilde{s} = 1$, the factor in (18) sets $\mathcal{P}_{\pi(x) \rightarrow x}(\gamma')$ to zero, such that terms A and

B vanish. For states “before” the start of the curve, one can consider the curve γ to be virtually extended backwards as a geodesic tangent to $\gamma'(0)$. This ensures that the transversality condition holds and the gradient $\nabla\Psi_{\text{NC}}$ is strictly orthogonal to $\mathcal{P}_{\pi(x)\rightarrow x}(\gamma')$. Hence, (21) simplifies to:

$$\dot{V}(x) = -k_{\text{NC}}^2 \|\nabla\Psi_{\text{NC}}(x)\|^2 - \frac{k_{\text{TC}}^2}{\beta(x)} (1 - \tilde{s}(x))C. \quad (22)$$

Since $\beta(x) > 0$ inside the tubular neighborhood, and $C > 0$ for $\tilde{s} < 1$, both terms in (22) are non-positive and vanish simultaneously only at the target state x^* . Therefore, the derivative \dot{V} is strictly negative definite on $\mathcal{D} \setminus \{x^*\}$. This implies that the equilibrium point x^* is locally asymptotically stable within the tubular neighborhood \mathcal{D} .

Based on this analysis, we conclude that the DS on the complete, connected Riemannian manifold M of Definition IV.2 is practically stable. We show the numerical stability of our method for randomized initial conditions in Section VI. For Lie groups G equipped with the distance metric (7), the stability analysis holds by identifying the geometry with the induced Log-Euclidean metric. In this flat geometry, parallel transport coincides with group translation, and the gradient of the normal energy potential corresponds to the Lie algebra error $\log(x^{-1}\pi(x))$. Consequently, the orthogonality condition $\langle \nabla\Psi_{\text{NC}}, \mathcal{P}_{\pi(x)\rightarrow x}(\gamma') \rangle = 0$ is naturally satisfied in the Lie algebra \mathfrak{g} , and metric distortion effects are effectively absent.

D. Phase Modulation

To further enhance the adaptability of the CDSM framework, we introduce a phase modulation layer which decouples the construction of the phase profile from that of the spatial profile. The phase and spatial profiles are parameterized using concatenated Bézier curves on $\mathbb{R}_{\geq 0}$ and the manifold, respectively. Adjusting the timing separately is beneficial in scenarios where, for example, the time profile should be optimized to remain within certain velocity limits, or collisions should be avoided with dynamic agents by slowing down or speeding up along the curve, while the spatial profile remains intact for user interpretability. Similar to a curve in Euclidean space, we can represent the evolution of the phase variable s of $\gamma(s)$ by a curve $\gamma^s(t)$, with end-time T and J segments:

$$s = \gamma^s(t) = \Psi(t/T)w, \quad t \in [0, T], \quad (23)$$

where w is a vector concatenation of all $w_{i,j}, \forall i \in \{1, 2, 3\}$ and $j \in \{1, 2, \dots, J\}$. Here, $\Psi(t)$ is a matrix containing Bernstein polynomial coefficients [8]. This representation allows us to flexibly define cost functions to build a phase and spatial profile separately. By restricting the phase s to be in the domain $[0, 1]$ and allowing no backwards motion along the curve, i.e. $(\gamma^s)'(t) > 0$, the time adaptation does not affect the stability analysis in IV-C. The DS gets affected by the phase modulation layer as the propagation term in Eq. (16) depends on the derivative of the curve. Since the spatial curve γ is parametrized by a phase variable $s(t)$, the chain rule yields

$$\gamma'(t) = \frac{\delta\gamma}{\delta s} \frac{\delta s}{\delta t} = \frac{\delta\gamma}{\delta s} (\gamma^s)'(t), \quad (24)$$

where $\frac{\delta\gamma}{\delta s}$ describes the derivative of the spatial curve with respect to the phase.

V. CDSM ON ROBOTICS-RELEVANT MANIFOLDS

The proposed CDSM is applicable to a broad class of Riemannian manifolds and Lie groups standard in robotics. In this section, we detail the construction of the exponential and logarithmic map, its distance and transformation for $SE(3)$ and S_{++}^n . Further details are available in [33] for $SE(3)$ and other Lie groups, and in [37] for S_{++}^n . Examples of other Riemannian manifolds and Lie groups can be found in our code. In addition, Section V-C provides a coupling mechanism between a DS of rigid body motions and a curve of variable damping matrices.

A. Dynamical System of 6-DoF Poses

Of particular interest for robotics is the group of rigid body motions, $SE(3)$. It is double-covered by the Lie group $G = \mathbb{H}_1 \ltimes \mathbb{R}^3$, where $\mathbb{H}_1 = \{q \in \mathbb{H} : \|q\| = 1\}$ is the group of unit quaternions, \mathbb{H} denotes the algebra of quaternions, and \ltimes denotes the semidirect product. Elements $g \in G$ are pairs (q, t) , where $q \in \mathbb{H}_1$ represents rotation, and $t \in \mathbb{R}^3$ is a global translation vector. The Lie algebra of this group is identified with $\mathfrak{se}(3)$, where elements are pairs $(\omega, v) \in \mathbb{R}^3 \times \mathbb{R}^3$, where ω is the angular velocity and v is the linear velocity, both expressed in the body frame. The exponential map sends $(\omega, v) \in \mathfrak{se}(3)$ to $(q, t) \in \mathbb{H}_1 \ltimes \mathbb{R}^3$ and the logarithmic map does the inverse. The exponential map $(q, t) = \exp(\omega, v)$, where q goes to identity as $\theta \rightarrow 0$, is given by

$$q = \cos(\theta/2) + \frac{\omega}{\theta} \sin(\theta/2), \quad t = V(\omega)v, \quad (25)$$

where $V(\omega)$ is the left Jacobian of $SO(3)$,

$$V(\omega) = I + \frac{1 - \cos\theta}{\theta^2} [\omega]_{\times} + \frac{\theta - \sin\theta}{\theta^3} [\omega]_{\times}^2, \quad \theta = \|\omega\|. \quad (26)$$

The logarithmic map $(\omega, v) = \log(q, t)$ is given by

$$\omega = \log(q), \quad v = V^{-1}(\omega)t, \quad (27)$$

with

$$V^{-1}(\omega) = I - \frac{1}{2} [\omega]_{\times} + \frac{1}{\theta^2} \left(1 - \frac{\theta \sin\theta}{2(1 - \cos\theta)} \right) [\omega]_{\times}^2. \quad (28)$$

We equip the Lie algebra $\mathfrak{g} \cong \mathfrak{se}(3)$ with a weighted inner product to handle the unit inconsistency between rotation (radians) and translation (meters). We introduce a characteristic length L_c and a weighting parameter $\eta = L_c^2$. Consistent with the general definition for Lie groups, we utilize the log-Euclidean distance, i.e. the *Screw Distance*:

$$d_G(g_1, g_2) = \|\log(g_1^{-1}g_2)\|_{\mathfrak{g}} = \sqrt{\eta \|\omega\|^2 + \|v\|^2}. \quad (29)$$

B. Symmetric Positive Definite Matrices S_{++}^n

Let S_{++}^n be the manifold of $n \times n$ symmetric positive definite matrices, often encoding stiffness matrices, damping matrices, or cost metrics in robotics,

$$S_{++}^n = \{P \in \mathbb{R}^{n \times n} \mid P = P^T \text{ and } P \succ 0\}. \quad (30)$$

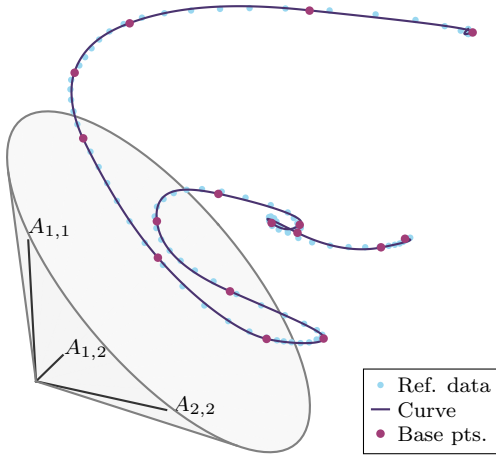


Fig. 4: Spline on \mathcal{S}_{++}^2 , which corresponds to the \mathcal{S}_{++}^2 -spline used in Fig. 5, obtained from the covariance. The axes indicate the diagonal ($A_{1,1}$ and $A_{1,2}$) and off-diagonal ($A_{1,2}$) terms of the 2×2 matrices.

Its tangent space $T_P \mathcal{S}_{++}^n$ at any point P , is the space of symmetric matrices \mathcal{S}^n . The closed-form expressions for the exponential and logarithmic maps are:

$$\exp_P(V) = P^{\frac{1}{2}} \expm(P^{-\frac{1}{2}} V P^{-\frac{1}{2}}) P^{\frac{1}{2}}, \quad (31)$$

$$\log_P(Q) = P^{\frac{1}{2}} \logm(P^{-\frac{1}{2}} Q P^{-\frac{1}{2}}) P^{\frac{1}{2}}, \quad (32)$$

with $\expm(\cdot)$ and $\logm(\cdot)$ being the matrix exponential and logarithm, respectively. The geodesic distance between two SPD matrices $P, Q \in \mathcal{S}_{++}^n$ is:

$$d_{\mathcal{S}_{++}^n}(P, Q) = \|\ln(P^{-\frac{1}{2}} Q P^{-\frac{1}{2}})\|_F = \left(\sum_{i=1}^n \ln^2 \lambda_i \right)^{\frac{1}{2}}, \quad (33)$$

where $\|\cdot\|_F$ is the Frobenius norm, and λ_i are the real, positive eigenvalues of $P^{-1}Q$. Parallel transport of $V \in \mathcal{S}^n$ from $P \in \mathcal{S}_{++}^n$ to $Q \in \mathcal{S}_{++}^n$ is computed as:

$$\mathcal{P}_{P \rightarrow Q}(V) = AVA^T, \quad \text{where } A = (QP^{-1})^{\frac{1}{2}}. \quad (34)$$

C. Coupling Poses in $SE(3)$ and Variable Matrices in \mathcal{S}_{++}^6

For the dressing task shown in Fig. 1, the curve $\gamma_{SE(3)}$ encodes the nominal trajectory for pulling the sleeve over the arm. Meanwhile, the dynamical system $f_{SE(3)}$ extends the velocity profile to states off the curve, $x \notin \gamma_{SE(3)}$, enabling robust handling of disturbances and arbitrary initial conditions on the group. Along $f_{SE(3)}$ encoding poses, we incorporate a continuous profile of variable gain matrices, $\gamma_{\mathcal{S}_{++}^n}$, that affect the resulting behavior. The required \mathcal{S}_{++}^n matrices at different poses can be provided by an expert or come from a human motor control-study [11]. As an accessible proxy for a \mathcal{S}_{++}^n profile, we consider the variability of the reference data, in form of covariance matrices, and invert them [19], [38], [39]. Intuitively, the larger the local variability observed in the data, the smaller the gains should be for returning to the reference under perturbations; mathematically, this is captured by defining the gain matrix as the inverse of the covariance matrix, which can be computed via eigenvalue decomposition.

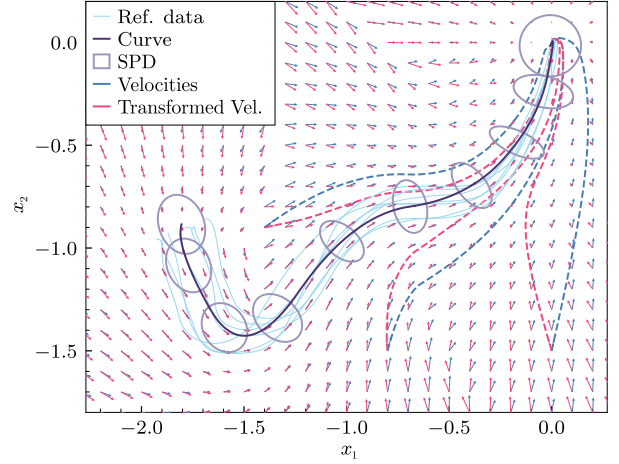


Fig. 5: Vector fields of a dynamical system in \mathbb{R}^2 without (blue) and with (pink) variable transformation matrices applied to the velocities, estimated from the reference data covariance. The velocity vectors not only change length but also direction, highlighting the presence of non-zero off-diagonal elements in the transformation matrices. To not affect the nominal behavior on the curve, we interpolate the transformation matrices toward identity as we get closer to the curve. The dashed lines are forward simulations of the unmodified and transformed velocities.

Although low covariance does not always justify high values of $\gamma_{\mathcal{S}_{++}^n}$ when near obstacles or in contact, this approach remains appropriate for free-space motions. Given a nominal pose curve, the idea is to estimate the covariance with respect to this curve. After aligning and resampling the reference data in time, \hat{X}^{ref} , consisting of K demonstrations, the mean and covariance at each phase s can be computed as,

$$\mu_s = \frac{1}{K} \sum_{x \in \hat{X}^{\text{ref}}(s)} \log_{\gamma(s)}(x), \quad (35)$$

$$\Sigma_s = \frac{1}{K} \sum_{x \in \hat{X}^{\text{ref}}(s)} (\log_{\gamma(s)}(x) - \mu_s)(\log_{\gamma(s)}(x) - \mu_s)^T. \quad (36)$$

We then compute the eigenvalue decomposition as $\Sigma_s = V^T \Lambda V$, where $V \in \mathbb{R}^{n \times n}$ is an orthonormal matrix of eigenvectors of Σ_s , and $\Lambda = \text{diag}(\lambda_1, \dots, \lambda_n) \in \mathbb{R}^{n \times n}$ is a real diagonal matrix of eigenvalues. While [19] encode all orientations in the tangent space at the goal quaternion, we estimate the covariance matrices in the nominal curve's moving tangent space and work with full 6×6 covariance matrices. Finally, we obtain variable velocity gain matrices, also referred to as damping matrices, as:

$$D_s = V \text{diag}\left(\frac{1}{\lambda_1 + d}, \dots, \frac{1}{\lambda_n + d}\right) V^T, \quad (37)$$

with damping gain d . This provides us with a set of phase-indexed damping matrices, $\{D_s\}$, to which the curve $\gamma_{\mathcal{S}_{++}^n}$ can be fitted as in Section V-B, and synchronized to the dynamical system, $f_{SE(3)}$, by phase.

In Fig. 4, an example is provided of a curve $\gamma_{\mathcal{S}_{++}^2}$ fitted using the covariances of the demonstrated data in \mathbb{R}^2 indicated in light-blue in Fig. 5. The effect of multiplying the velocity output of the dynamical system, $f_{SE(3)}$, with the transforma-

TABLE I: Quantitative results on the LASA dataset mapped to the S^2 -manifold.

	Trajectory distance	Path distance (x_0 randomized)	Success rate	Computation time trajectory [s]	Train/Fitting time [s]
CDSM (ours)	0.0042 \pm 0.0087	0.0339 \pm 0.1292	1.0	0.0039 \pm 0.0006	1.26 \pm 0.16
Lieflows	0.0131 \pm 0.0072	0.0869 \pm 0.5574	0.81	0.5157 \pm 0.0281	1324.85 \pm 8.47
PUMA	0.0112 \pm 0.0044	0.0982 \pm 0.2092	1.0	0.0562 \pm 0.0111	204.03 \pm 10.63

tion matrices from $\gamma_{S^2_+}$ is visible in the vector field of Fig. 5 on both the direction and the length of the velocity vectors. As we want the nominal behavior to remain unaffected, we interpolate these matrices toward identity as we approach the curve (see Fig. 5). Inspecting the generated trajectories shows that, as the demonstrated trajectories get closer to each-other, i.e. the covariance decreases, the transformed velocities induce a stronger attraction toward the curve than the original velocities. This behavior persists until the trajectory is sufficiently close to the curve, at which point the interpolation toward the identity is activated.

VI. EXPERIMENTS

To verify the applicability of CDSM, we first provide a comparison on S^2 against LieFlows and PUMA in Section VI-A, followed by an illustrative example of curve fitting in $SO(3)$ and the effect of the phase modulation layer. We then demonstrate our approach on a dressing task with a 7-axis torque-controlled Franka robot, adapting online to the configuration of a human arm, and further showcase its cross-platform applicability on a mobile manipulator dressing a mannequin arm.

A. LASA Dataset on S^2

We compare our approach, CDSM, with LieFlows [1] and PUMA [5] on the LASA dataset [40] mapped to S^2 . The LASA dataset consists of handwritten shape trajectories. We use 26 unimodal non-intersecting shapes, each comprising 7 demonstrations. Both methods are evaluated using the following metrics:

- *Trajectory distance*: Given a demonstration i sampled with Δt^i and initial point x_0^i . The trajectory distance indicates the average geodesic distance on S^2 between the first 100 timesteps of the DS-generated trajectory and the closest demonstration using an identical x_0^i and Δt^i for the DS. It reflects how closely the DS follows the demonstration in both space and time.
- *Path distance*: From a set of randomly sampled initial points $x_0 = \exp_{x_g}(\log_{x_g}(x_0^i) + 2(r-1))$, where $r \in [0, 1)$ and goal position x_g lies on the manifold, the DS is forward simulated for $N = 200$ timesteps and $\Delta t = 0.01$ s. The path distance is defined as the mean geodesic distance between each point of the trajectory and the nearest discrete point in the demonstration set, and gives a measure of attraction towards the region where the demonstrations lie.
- *Success rate*: Given the trajectories generated from randomly sampled initial points, we define the success rate

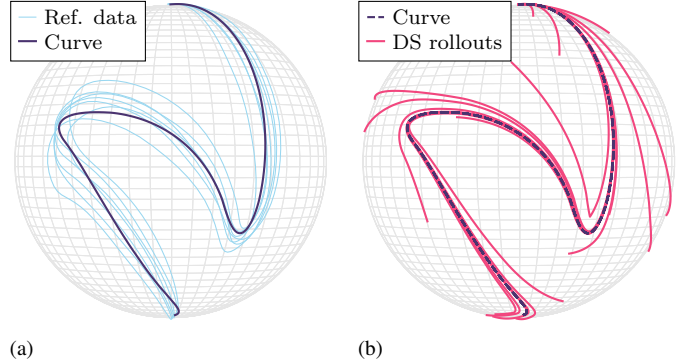


Fig. 6: LASA N-Shape on S^2 . (a) Curve fitting. (b) DS rollouts.

as the ratio of successful runs over all runs. A trajectory is considered successful if the final state satisfies $d_M(x(T), x_g) \leq 0.2$ where $T = N\Delta t$.

- *Computation time trajectory*. The wall-clock time required to forward-simulate a batch of 7 randomly sampled initial conditions per shape, averaged over all 26 shapes.
- *Train/Fitting time*: The wall-clock time required to train the NN of Lieflows or PUMA for a single shape, or, for CDSM, to fit the spline and construct the DS.

The curves for CDSM are constructed using 6 spline segments, optimized with a SLSQP solver. The initial guess is generated via a naive least-squares fit in a single tangent space, perturbed with random noise of maximum amplitude 10^{-4} . For CDSM, the DS-parameters are set to $k_{NC} = 3.0$, $k_{TC} = 1.0$ and $k_g = 8$. For Lieflows and PUMA, training is performed for 10,000 iterations, with all other parameters set to their default values as specified in their respective open-source implementations. All experiments are conducted on a standard laptop (Intel i7-12700H CPU).

Analyzing the trajectory distance in Table I and Fig. 6, we observe that the proposed CDSM most accurately captures both the temporal and spatial profiles of the demonstrations on S^2 , when initialized at the demonstrated starting points. While Lieflows and PUMA also achieve low trajectory distances, CDSM significantly outperforms both methods in path distance for randomly sampled initial positions, highlighting its robustness in out-of-distribution scenarios. This improved performance arises from CDSM's ability to converge more rapidly toward the demonstration region by balancing attraction to the curve and tangential progression along the curve. Specifically, CDSM explicitly modulates tangential and normal velocities, enabling faster convergence to regions with richer information and more accurate adherence to the desired movement profile. In contrast, Lieflows occasionally fails to reach the goal within $N = 200$ steps, either due to slow local progression or convergence to the antipodal pole $x_g = (0, 0, -1)$.

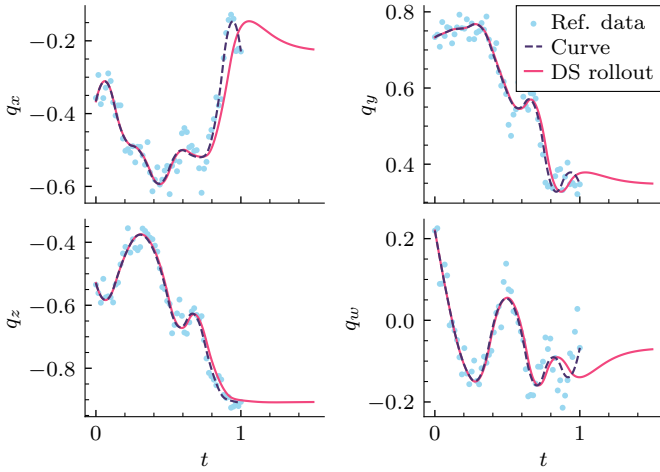


Fig. 7: Reference data, curve, and DS rollout on $SO(3)$, plotted over time, with $k_{TC} = 1$, $k_{NC} = 2$, and $k_g = 8$. Note the damped motion near the goal due to (18).

All evaluated methods demonstrate real-time action querying capabilities, with average latencies of (0.15 ± 0.06) ms for CDSM, (12.64 ± 6.3) ms for Lieflows and (0.25 ± 0.027) ms for PUMA, confirming their suitability for real-world applications. Notably, CDSM outperforms the other methods in forward simulation efficiency: its computation time for a trajectory of $N = 200$ steps is approximately one order of magnitude faster than PUMA and two orders of magnitude faster than Lieflows. This efficiency enables CDSM to provide real-time trajectory predictions that are useful for robot path planning, and also facilitates integration with high-level planners that might need to simultaneously evaluate multiple dynamical systems in future studies. Additionally, CDSM achieves rapid shape fitting in just (1.26 ± 0.16) s on average, making it capable of real-time DS generation. In contrast, Lieflows and PUMA require several minutes of training per shape, limiting their applicability in changing environments.

B. Curve Optimization on $SO(3)$

As previously observed for LASA on S^2 using trajectory distance, the proposed dynamical system accurately tracks both the spatial profile as well as the timing of the reference data. This is illustrated in Fig. 7, which shows a forward simulation of CDSM on $SO(3)$ data over time and highlights the effect of (18), which causes a damped movement to the goal point. The parameter k_g can be adjusted to suit different applications.

C. Phase Modulation

When preserving the time profile is undesired, a phase modulation layer enables temporal optimization while maintaining a fixed, interpretable spatial profile. In Fig. 8, a phase modulation profile is shown which optimizes the time to reach the goal while adhering to speed constraints, $\|v(t)\| \leq \bar{v}$, with the velocity $v(t)$ defined in the local tangent space $T_{x(t)}S^2$ and limit $\bar{v} = 3.0$. The phase modulation curve, γ^s , consists of 10 segments. To prevent backward motion

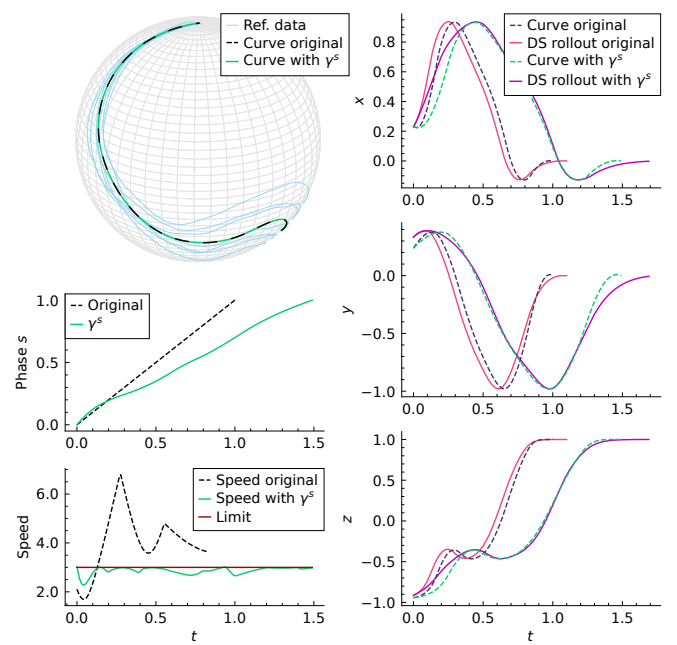


Fig. 8: The effect of an optimization of the phase modulation layer with an existing spatial curve in S^2 where constraints ensure that the speed, $\|v(t)\|$, is below the limit $\bar{v} = 3.0$, and $(\gamma^s)'(t) \geq 0$.

along the spatial profile, we enforce a constraint ensuring that the derivative of the phase curve, $(\gamma^s)'(t) = \frac{\delta s}{\delta t}$, remains strictly positive. As observed in Fig. 8, the spatial profile of the curve on S^2 is preserved, while the temporal profile is modified to ensure that the speed remains below the prescribed maximum, in contrast to the original speed profile. Comparing the phase-modulated curve γ^s with the original curve shows that not only the time to reach the goal, but also the velocity profile along the curve and of the DS rollouts is altered. The introduction of the phase modulation layer preserves the system's numerical stability while effectively modifying the trajectory characteristics. Computation times for fitting the curve γ^s are (1.65 ± 0.49) s averaged over all 26 S^2 -shapes using 10 segments, and (0.39 ± 3.87) ms for querying an action. Future work could explore extending the phase modulation to enable collision avoidance in dynamic environments, as well as learning phase modulation profiles directly from real-world data.

D. Human Arm Dressing

To evaluate the real-world applicability of the proposed DS and variable damping framework, we deploy our method on a robotic dressing task (see Fig. 9). From previous studies addressing such task, e.g. [41], [42], we conclude that this scenario demands fast and continuous online adaptation, as the system must simultaneously ensure human-safe compliance, track the human arm online, and achieve the precision necessary for garment manipulation.

1) *Experimental Setup and Sensing*: We run the experiments on a Franka robot, utilizing Cartesian impedance control. The control loops for high- and low-level commands run at 1 kHz. For arm tracking, we use an Intel RealSense D415

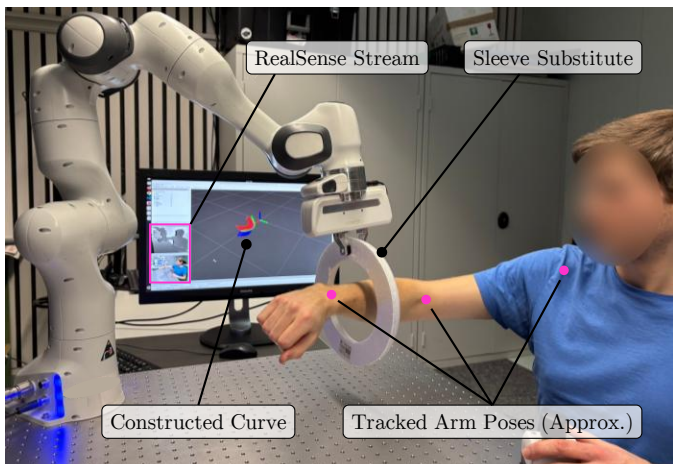


Fig. 9: Setup of the arm dressing experiment. The RealSense camera is positioned near the viewpoint of this photo.

camera and perform initial processing with MediaPipe [43]. We extract the 3D coordinates of the user’s wrist, elbow, and shoulder to construct a composite quadratic Bézier spline with two segments online. This spline defines the trajectory of end-effector poses in $SE(3)$ along which the robot follows the arm.

2) *Controller Formulation:* The following variable impedance control law governs the interaction:

$$\tau(t) = J^T D_c \left(D(x(t)) \dot{x}_d - \dot{x}(t) \right) \quad (38a)$$

$$= J^T D_c \left(\gamma_{S_{++}^n}(\tilde{s}(x(t))) f_{SE(3)}(x(t)) - \dot{x}(t) \right), \quad (38b)$$

where $\tau(t)$ is the commanded torque, J is the geometric Jacobian, $D_c \in S_{++}^6$ represents the fixed damping gain of the Cartesian controller, \dot{x}_d and $\dot{x}(t)$ are the desired and current twist, respectively, and $f_{SE(3)}$ is the nominal DS output. The variable damping matrix $D(x(t))$ is updated at 1 kHz alongside the DS, and applied to the desired twist. For fixed damping, we simply omit $D(x(t))$. This control law is augmented with gravity compensation and null-space control to keep the robot in singularity-free regions of the workspace. The parameters of the $f_{SE(3)}$ are chosen to be $k_{TC} = 1$, $k_{NC} = 2$, $k_g = 0$, $L_c = 0.01$ for closest point projection, and $L_c = 0.1$ for any other operations involving distance computation.

3) *Experimental Cases:* We consider five scenarios: (i) dressing a static arm, (ii) perturbations before the garment (represented by the white ring) is around the arm, (iii) perturbations during movement along a static arm, (iv) user-induced perturbations during execution, in which the robot is physically displaced while the user simultaneously moves their arm to a different configuration, and (v) dressing a moving arm, where the user actively adjusts their wrist, elbow, and shoulder poses in real time. Here, for visual interpretability, variable damping matrices are constructed as a curve of diagonal matrices in S_{++}^6 , though our framework supports full S_{++}^6 matrices. During the experiment, the gains in $D(x(t))$ vary smoothly from 0.5 to 2 based on the progress along the spline. This results in an intentional increase in velocity gains as

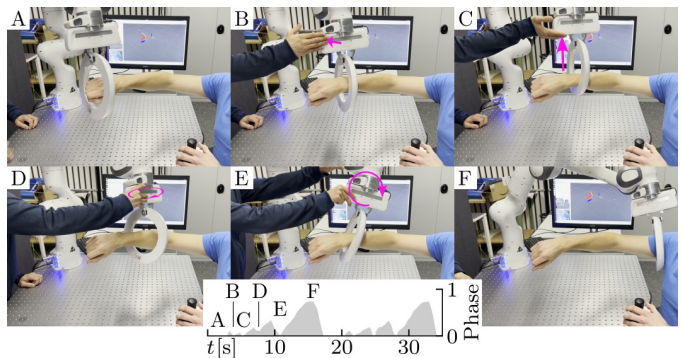


Fig. 10: Various snapshots of the scene during the dressing task. Frames A and F show the beginning and end of the first of two repeated runs, respectively. The other frames show different kinds of perturbations: B push laterally, C push up, D twist counter clockwise, E tilt forward.

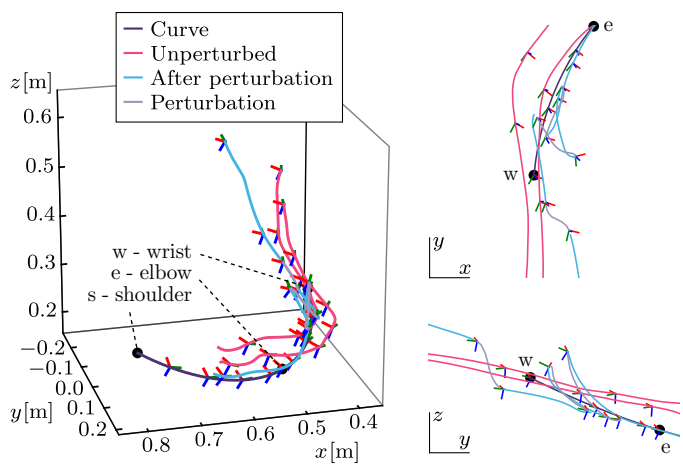


Fig. 11: A snapshot of the curve for a tracked steady arm (dark violet) with two trajectories of the robot when not pushed (pink). We also show some perturbations (gray) and the behavior of the robot after the perturbations (light blue). The world frame is aligned with the robot base frame. Due to the human arm not being perfectly still, the curve moved a little throughout the experiment, and hence the illustrated curve is only a snapshot.

the end-effector approaches the shoulder. As mentioned in Section V-C, the variable damping matrices obtained from $\gamma_{S_{++}^n}$ were applied fully when the distance from the curve was greater than a threshold of 0.05 for the experiment in Fig. 11 and 0.01 for the experiment in Figs. 10, 12, 13, and interpolated toward identity when closer to the curve.

For the plots presented in this paper, we focus on the scenario of a stationary human arm, while introducing perturbations by pushing or pulling the robot during the dressing motion. This analysis includes both fixed and variable damping conditions. Fig. 10 shows snapshots of an experiment using a DS in $SE(3)$ with variable damping, captured at key time points. Additionally, the supplementary video¹ demonstrates all five scenarios, where a static as well as a moving arm is dressed.

4) *Human Arm Dressing with a Mobile Manipulator:* To verify the applicability of our approach across different robotic

¹Video available at: [cd-sm.github.io](https://github.com/cd-sm).

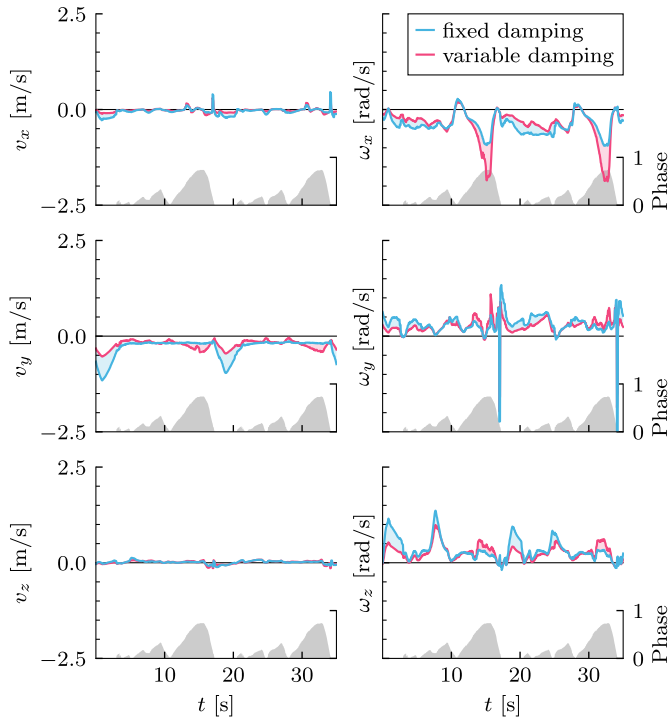


Fig. 12: Robot moving along a static arm with perturbations to position and orientation, repeated twice. The experiment is performed with the damping varying linearly with the phase along the nominal curve from 0.5 to 2. The resulting twist outputs of the DS are plotted in pink, the phase in gray and the twists when using a fixed damping are in blue.

platforms, and to observe its performance in the presence of internal perturbations caused by the physical limitations of the robotic system, we demonstrate it on a mobile manipulator comprising a Kinova Gen3 Lite mounted on a Clearpath Dingo base (see Fig. 14). Given that the mobile manipulator only accepts joint velocity commands, the poses generated by $f_{SE(3)}$ are directly fed into the low-level geometric controller [44]. Illustrative experiments were conducted using several arm poses of a mannequin arm and starting poses of the robot. Joint velocity commands and high-level commands are sent at 40 Hz and 20 Hz respectively, and the arm coordinates and robot base pose are tracked online with a VICON motion capture system.

E. Results and Discussion

In Fig. 11, the robot approaches the static arm from some distance away and continues to follow the curve, which is continuously updated based on the tracked arm pose. Imperfect alignment with the curve is caused by various factors: (a) the arm is not perfectly still, (b) contact between the foam ring and the arm due to inaccuracies in the spline offsets used for its construction, and (c) camera noise on the arm pose tracking. Note that (a) is a significant factor in Fig. 11, which directly explains why the perturbed trajectories appear to converge to the curve quicker than the unperturbed ones. The curve shown in Fig. 11 is a snapshot of the curve when perturbations were applied, and the curve varied a little throughout the experiment due to human arm movements. We further note that for the

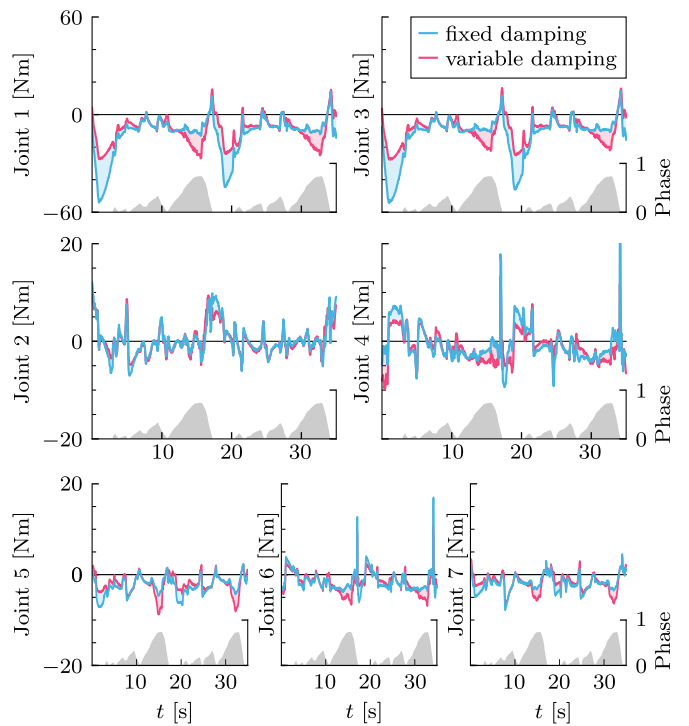


Fig. 13: Resulting torque values of the twists applied in Fig. 12 over time, with the phase in gray. The torque commands from (38) with $D_c = \text{diag}(90, 90, 90, 4, 4, 4)$ are shown in pink, while the torque commands with a fixed damping are in blue.

experiment the robot is unable to reach the very end of the curve because it is impeded by the armpit, as observed in Fig. 1. When external perturbations are applied, observed as gray lines in Fig. 11, the system complies and continues to follow the DS afterwards, converging to the curve, as indicated in light blue.

Next, we analyze the effect of variable damping on the twists, joint torques, and human-observed stiffness of the movement. In Figs. 12 and 13, the twist and joint torque values are shown with fixed and variable damping, where the perturbation sequence as in frames A-F in Fig. 10 is repeated twice. Joint torques under variable damping are applied to the robot, while those under fixed damping are derived for comparison, because identical human disturbances cannot be replicated. When variable damping is enabled, the twist outputs from $f_{SE(3)}$ are modified based on the current phase along the nominal curve. In the particular example of Fig. 12, a linear scheduling of the damping gain from 0.5 to 2 across the phase leads to lower twists early on and increased twist magnitudes at higher phases. The increased damping strength from wrist to shoulder renders the robot softer and less aggressive during the approach phase and during early stages of the nominal curve, and stiffer and more reactive closer to the shoulder, as observed from the command torque values in Fig. 13 and perceived by the users.

During experiments, occasional jumps in the tracked curve were observed due to the inherent limitations of the vision system and occlusions. However, due to the fast recomputation of our system and the compliant nature of our controller,

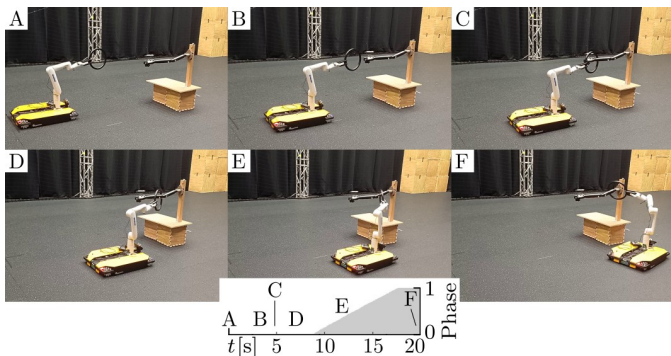


Fig. 14: The dressing task executed by a mobile manipulator consisting of a Kinova Gen3Lite mounted on a Clearpath Dingo base. Frames A and F indicate the start and end-pose, respectively.

these discontinuities did not result in excessively jerky motions or safety hazards for the human subject. Whenever tracking confidence reported by MediaPipe was below 0.9, the last good arm pose estimate was used.

On the mobile manipulator, the proposed CDSM executes the dressing task of a mannequin arm from different initial positions of the robot’s base and configurations of the mannequin arm, as observed in the video and Fig. 14. When reaching the elbow joint of the mannequin, the mobile manipulator must reconfigure both its mobile base and arm before continuing the motion of the end-effector. This demonstrates the system’s ability to handle not only external disturbances (Fig. 10), but also internal perturbations caused by the physical constraints of the robotic platform, emphasizing the advantage of CDSM over a time-based motion primitives. Due to wheel slip with the omnidirectional wheels, as well as additional damping induced by the low-level controller, the tracking accuracy was diminished with respect to the experiments on the Franka robot. Incorporating visual feedback on the current ring or garment placement with respect to the human arm could make the dressing task more realistic for users [41]. Nevertheless, the experiment highlights our framework’s cross-platform capabilities and its potential use in real-world at-home scenarios.

VII. LIMITATIONS AND CONCLUSION

We proposed CDSM, a framework for generating a curve-induced dynamical system on Riemannian manifolds and Lie groups in real-time. The dynamical system combines an attracting normal vector towards a curve and a propagating tangential vector in the direction of the curve, and we provide a stability analysis of the proposed method. We analyze the performance using quantitative experiments, where CDSM outperforms Liefloows and PUMA on an S^2 dataset in terms of trajectory and path distance, as well as generation and query time. In addition, we provide experiments with a manipulator on a dressing task varying both poses on $SE(3)$ and damping matrices on S_{++}^6 online, and demonstrate cross-platform applicability of the approach by performing the dressing task with a mobile manipulator.

Our current experiments are limited to uni-modal demonstrations and movements, but the proposed approach naturally

extends to multimodal scenarios. One possible extension involves defining a single DS from multiple curves and simply projecting toward the closest curve for any given query point. Alternatively, multiple DSs, each associated with its own curve, could be generated, with the most relevant DS selected dynamically based on the observed scenario. Additionally, we introduced a coupling between a pose-based dynamical system and varying S_{++}^n matrices representing the velocity gains. In future work, these matrices and the parameters of the dynamical system could be learned from human data [11], enabling adaptable and human-like movements. When adapting the damping matrix online, we assume gradual changes to preserve the stability of the closed-loop robotic system. Under this assumption, a passivity analysis could be performed to verify stability during damping adaptation. To further enhance system robustness, we suggest introducing an energy-budget constraint for the Cartesian impedance controller [45], [46]. This constraint would cap the maximum potential energy of the system, ensuring that the proportional term of the controller only steers toward poses that comply with the energy limit, thereby safeguarding against instability.

REFERENCES

- [1] J. Urain, D. Tateo, and J. Peters, “Learning stable vector fields on Lie groups,” *IEEE Robotics and Automation Letters*, vol. 7, no. 4, pp. 12 569–12 576, 2022.
- [2] J. Zhang, H. B. Mohammadi, and L. Rozo, “Learning Riemannian stable dynamical systems via diffeomorphisms,” in *Proc. Conference on Robot Learning (CoRL)*, 2022.
- [3] H. Ding, N. Jaquier, J. Peters, and L. Rozo, “Fast and robust visuomotor Riemannian flow matching policy,” *IEEE Transactions on Robotics*, vol. 41, pp. 5327–5343, 2025.
- [4] R. T. Q. Chen and Y. Lipman, “Flow matching on general geometries,” in *Proc. International Conference on Learning Representations (ICLR)*, 2024.
- [5] R. Pérez-Dattari, C. Della Santina, and J. Kober, “Puma: Deep metric imitation learning for stable motion primitives,” *Advanced Intelligent Systems*, vol. 6, no. 11, p. 2400144, 2024.
- [6] C. Mancinelli and E. Puppo, “Splines on manifolds: A survey,” *Computer Aided Geometric Design*, vol. 112, p. 102349, 2024.
- [7] M. Watterson, S. Liu, K. Sun, T. Smith, and V. Kumar, “Trajectory optimization on manifolds with applications to quadrotor systems,” *The International Journal of Robotics Research*, vol. 39, no. 2-3, pp. 303–320, 2020.
- [8] Y. Li and S. Calinon, “From movement primitives to distance fields to dynamical systems,” *IEEE Robotics and Automation Letters*, vol. 10, no. 9, pp. 9550–9556, 2025.
- [9] W. Yao, *Guiding Vector Fields for Robot Motion Control*, ser. Springer Tracts in Advanced Robotics. Springer, 2023, vol. 154.
- [10] B. Lee, Y. Lee, J. Ha, and F. C. Park, “Behavior-controllable stable dynamics models on riemannian configuration manifolds,” *IEEE Transactions on Robotics*, 2025.
- [11] A. Ajoudani, C. Fang, N. G. Tsagarakis, and A. Bicchi, “A reduced-complexity description of arm endpoint stiffness with applications to teleimpedance control,” in *Proc. IEEE/RSS International Conference on Intelligent Robots and Systems (IROS)*, 2015.
- [12] X. Chen, Y. Michel, and D. Lee, “Closed-loop variable stiffness control of dynamical systems,” in *Proc. IEEE-RAS International Conference on Humanoid Robots (Humanoids)*, 2021, pp. 163–169.
- [13] N. Geiger, T. Asfour, N. Hogan, and J. Lachner, “Diffusion-based impedance learning for contact-rich manipulation tasks,” no. arXiv:2509.19696, 2025.
- [14] J. Bradbury, R. Frostig, P. Hawkins, M. J. Johnson, C. Leary, D. Maclaurin *et al.*, “JAX: composable transformations of Python+NumPy programs,” 2018. [Online]. Available: <http://github.com/google/jax>
- [15] M. Blondel, Q. Berthet, M. Cuturi, R. Frostig, S. Hoyer, F. Linares-López *et al.*, “Efficient and modular implicit differentiation,” *Advances in neural information processing systems*, vol. 35, pp. 5230–5242, 2022.

- [16] Y. Hu, F. J. Abu-Dakka, F. Chen, X. Luo, Z. Li, A. Knoll, and W. Ding, "Fusion dynamical systems with machine learning in imitation learning: A comprehensive overview," *Information Fusion*, vol. 108, p. 102379, 2024.
- [17] Y. Lipman, R. T. Chen, H. Ben-Hamu, M. Nickel, and M. Le, "Flow matching for generative modeling," in *Proc. International Conference on Learning Representations (ICLR)*, 2023.
- [18] J. Urain, N. Funk, J. Peters, and G. Chalvatzaki, "SE(3)-diffusionfields: Learning smooth cost functions for joint grasp and motion optimization through diffusion," in *Proc. IEEE International Conference on Robotics and Automation (ICRA)*, 2023.
- [19] M. Saveriano, F. J. Abu-Dakka, and V. Kyrki, "Learning stable robotic skills on Riemannian manifolds," *Robotics and Autonomous Systems*, vol. 169, p. 104510, 2023.
- [20] S. Fiori, I. Cervigni, M. Ippoliti, and C. Menotta, "Synthetic nonlinear second-order oscillators on Riemannian manifolds and their numerical simulation," *Discrete & Continuous Dynamical Systems - B*, vol. 27, no. 3, p. 1227, 2022.
- [21] L. Koutras and Z. Doulgeri, "A correct formulation for the orientation dynamic movement primitives for robot control in the cartesian space," in *Proc. Conference on Robot Learning (CoRL)*, 2020.
- [22] A. Ude, B. Nemeč, T. Petrić, and J. Morimoto, "Orientation in cartesian space dynamic movement primitives," in *Proc. IEEE International Conference on Robotics and Automation (ICRA)*, 2014.
- [23] M. Saveriano, F. Franzel, and D. Lee, "Merging position and orientation motion primitives," in *Proc. IEEE International Conference on Robotics and Automation (ICRA)*, 2019.
- [24] F. J. Abu-Dakka, M. Saveriano, and V. Kyrki, "A unified formulation of geometry-aware discrete dynamic movement primitives," *Neurocomputing*, vol. 598, p. 128056, Sep. 2024.
- [25] L. Rozo and V. Dave, "Orientation probabilistic movement primitives on Riemannian manifolds," in *Proc. Conference on Robot Learning (CoRL)*, 2022.
- [26] V. M. Gonçalves, L. C. Pimenta, C. A. Maia, B. C. Dutra, and G. A. Pereira, "Vector fields for robot navigation along time-varying curves in n -dimensions," *IEEE Transactions on Robotics*, vol. 26, no. 4, pp. 647–659, 2010.
- [27] C. Wu, J. Chen, D. Jeltsema, and C. Dai, "Guidance vector field encoding based on contraction analysis," in *European Control Conference (ECC)*. IEEE, 2018.
- [28] P. Y. Li and R. Horowitz, "Passive velocity field control (PVFC). Part II. Application to contour following," *IEEE Transactions on Automatic Control*, vol. 46, no. 9, pp. 1360–1371, 2002.
- [29] N. Figueroa and A. Billard, "Locally active globally stable dynamical systems: Theory, learning, and experiments," *The International Journal of Robotics Research*, vol. 41, no. 3, pp. 312–347, 2022.
- [30] N. Jaquier, L. Rozo, and T. Asfour, "Unraveling the single tangent space fallacy: An analysis and clarification for applying Riemannian geometry in robot learning," in *Proc. IEEE International Conference on Robotics and Automation (ICRA)*, 2024.
- [31] J. M. Lee, *Introduction to Smooth Manifolds*, 2nd ed., ser. Graduate Texts in Mathematics. Springer, 2013, no. 218.
- [32] —, *Introduction to Riemannian Manifolds*, ser. Graduate Texts in Mathematics. Springer, 2018, vol. 176.
- [33] J. Solà, J. Deray, and D. Atchuthan, "A micro Lie theory for state estimation in robotics," no. arXiv:1812.01537, 2021.
- [34] T. Lee, M. Leok, and N. H. McClamroch, "Geometric tracking control of a quadrotor UAV on SE(3)," in *49th IEEE Conference on Decision and Control (CDC)*, 2010.
- [35] F. Bullo and A. D. Lewis, *Geometric Control of Mechanical Systems: Modeling, Analysis, and Design for Simple Mechanical Control Systems*, ser. Texts in Applied Mathematics. Springer, 2005, vol. 49.
- [36] M. P. do Carmo, *Riemannian Geometry*, ser. Mathematics. Theory & Applications. Birkhäuser Boston, 1992.
- [37] X. Pennec, P. Fillard, and N. Ayache, "A Riemannian framework for tensor computing," *International Journal of Computer Vision*, vol. 66, no. 1, pp. 41–66, 2006.
- [38] K. Kronander and A. Billard, "Learning compliant manipulation through kinesthetic and tactile human-robot interaction," *IEEE Transactions on Haptics*, vol. 7, no. 3, pp. 367–380, 2014.
- [39] J. Silvério, Y. Huang, F. J. Abu-Dakka, L. Rozo, and D. G. Caldwell, "Uncertainty-aware imitation learning using kernelized movement primitives," in *Proc. IEEE/RSJ International Conference on Intelligent Robots and Systems (IROS)*, 2019.
- [40] S. M. Khansari-Zadeh and A. Billard, "Learning stable nonlinear dynamical systems with gaussian mixture models," *IEEE Transactions on Robotics*, vol. 27, no. 5, pp. 943–957, 2011.
- [41] Y. Wang, Z. Sun, Z. Erickson, and D. Held, "One Policy to Dress Them All: Learning to Dress People with Diverse Poses and Garments," Jun. 2023.
- [42] G. Franzese, R. Prakash, C. Della Santina, and J. Kober, "Generalizable motion policies through keypoint parameterization and transportation maps," *IEEE Transactions on Robotics*, 2025.
- [43] C. Lugaresi, J. Tang, H. Nash, C. McClanahan, E. Uboweja, M. Hays *et al.*, "MediaPipe: A Framework for Building Perception Pipelines," Jun. 2019.
- [44] M. Spahn, M. Wisse, and J. Alonso-Mora, "Dynamic optimization fabrics for motion generation," *IEEE Transactions on Robotics*, vol. 39, no. 4, pp. 2684–2699, 2023.
- [45] K. Kronander and A. Billard, "Passive interaction control with dynamical systems," *IEEE Robotics and Automation Letters*, vol. 1, no. 1, pp. 106–113, Jan. 2016.
- [46] J. Lachner, F. Allmendinger, E. Hobert, N. Hogan, and S. Stramigioli, "Energy budgets for coordinate invariant robot control in physical human-robot interaction," *The International Journal of Robotics Research*, vol. 40, no. 8-9, pp. 968–985, 2021.